

## Construction of Bi<sub>2</sub>WO<sub>6</sub> with oxygen vacancies and investigation on mechanisms of significantly enhanced photocatalytic activity

Wen An<sup>a</sup>, Shaomang Wang<sup>a,\*</sup>, Yang Fu<sup>a</sup>, Yuan Guan<sup>b</sup>, Zhongyu Li<sup>b,\*</sup>, Tao Xu<sup>a</sup>, Haoran Wang<sup>a</sup>

<sup>a</sup>School of Environment and Safety Engineering, Changzhou University, Changzhou, Jiangsu 213164, China, Tel. +8651986330086, emails: gywsm@cczu.edu.cn (S.M. Wang), 2914433428@qq.com (W. An), 895710489@qq.com (Y. Fu), 1534078935@qq.com (T. Xu), 3193311802@qq.com (H.R. Wang)

<sup>b</sup>Jiangsu Province Key Laboratory of Fine Petrochemical Engineering, School of Petrochemical Engineering, Changzhou University, Changzhou, Jiangsu 213164, China,

Received 30 May 2020; Accepted 19 November 2020

### ABSTRACT

Bi<sub>2</sub>WO<sub>6</sub> nanosheets with gradient oxygen vacancies were synthesized by acetic acid solvothermal and subsequent calcination. The photocatalytic activity of the calcined Bi<sub>2</sub>WO<sub>6</sub> was significantly enhanced. The calcination regulated the oxygen vacancy in Bi<sub>2</sub>WO<sub>6</sub>. Oxygen vacancy defects helped to adjust the band structure and change the surface chemical state. At the same time, the electrons were the main charge carriers of the *n*-type semiconductor Bi<sub>2</sub>WO<sub>6</sub>. Part of the electrons was captured by the oxygen vacancies to promote the separation of the holes. Some of the electrons reacted with oxygen to generate <sup>•</sup>O<sub>2</sub><sup>-</sup>. The h<sup>+</sup> and <sup>•</sup>O<sub>2</sub><sup>-</sup> were the main active species that degraded rhodamine B. Among them, Bi<sub>2</sub>WO<sub>6</sub> with 1 h of calcination at 315°C (Bi<sub>2</sub>WO<sub>6</sub>-315°C 1 h) exhibited the optimal photocatalytic activity. The degradation velocity of rhodamine B over Bi<sub>2</sub>WO<sub>6</sub> was 21.4 times that of Bi<sub>2</sub>WO<sub>6</sub> under the same reaction condition.

*Keywords:* Photocatalysis; Bismuth tungstate; Defect; Oxygen vacancy; Radical reactions

### 1. Introduction

In recent years, dyeing wastewater has become more and more serious to the water environment with the increase in dye production [1–4]. Semiconductor-based photocatalytic technology has been proved to be a sustainable technology for purifying dyeing wastewater [5–9]. The rapid recombination of carriers and the narrow absorption range of sunlight are the main bottlenecks of most photocatalysts [9–13].

Bi-based photocatalysts, for example, Bi<sub>2</sub>O<sub>3</sub>, Bi<sub>2</sub>MoO<sub>6</sub>, BiVO<sub>4</sub> and Bi<sub>2</sub>WO<sub>6</sub> have been attracted great attention due to their obvious visible light response and promising

application of solar energy [14,15]. Bismuth tungstate (Bi<sub>2</sub>WO<sub>6</sub>) is a simple Aurivillius type compound whose layered structure consists of alternating (Bi<sub>2</sub>O<sub>2</sub>)<sup>2+</sup> and (WO<sub>4</sub>)<sup>2-</sup> octahedral layers with excellent visible-light photocatalytic activity [16–18]. However, it still faces the problems of narrow solar spectrum response range and low quantum efficiency [19–21]. Therefore, it is currently to be solved to widen the light absorption range of Bi<sub>2</sub>WO<sub>6</sub> to the visible light region and suppress photo-generated electron-hole recombination. Many strategies have been proposed to enhance its visible-light absorption and promote the separation and transfer of photogenerated carriers, such as

\* Corresponding authors.

loading precious metals, building heterojunctions [22], and doping ionic elements [23–25]. In all of these strategies, defects can generally expand the photoresponse range by reducing the bandgap and act as photoinduced charge traps, inhibit electron-hole recombination, and extend carrier lifetime. But too many oxygen vacancies will also become the center of electron and hole recombination.

In recent years, some investigations on structural defects in  $\text{Bi}_2\text{WO}_6$  have been reported. For example, C was incorporated into  $\text{Bi}_2\text{WO}_6$  nanospheres to introduce oxygen vacancies by the GO-mediated hydrothermal method [26]. Oxygen vacancies generated by carbon doping can become shallow potential traps for photo-generated electron-hole pairs, speeding up the transfer of surface charges and extending the recombination time of electrons and holes. Hao et al. used  $\text{Nb}^{5+}$  to partially substitute  $\text{W}^{6+}$  constructing oxygen vacancies. Oxygen vacancies improve charge separation efficiency and expand the light absorption range [27]. Xu et al. [28] fabricated oxygen-deficient  $\text{Bi}_2\text{WO}_{6-x}$  nanoplates through an alkali etching method, which widens the light absorption range and improves the photocatalytic activity.  $\text{Bi}_2\text{WO}_6$  with defects can also be synthesized by the  $\text{NaBH}_4$  etching method [29,30]. However, few people regulate oxygen vacancies by directly calcining in air.

Different from the predecessors, in this study,  $\text{Bi}_2\text{WO}_6$  with oxygen vacancies was synthesized by hydrothermal method using acetic acid as a solvent, and then the oxygen vacancies were reduced by calcination, and the photocatalytic activity of  $\text{Bi}_2\text{WO}_6$  was adjusted [18,25,26]. A series of physical and chemical characterizations of the samples and photocatalytic activity tests for rhodamine B (RhB) removal from water were performed. The relationship between the structures of these samples and their photocatalytic activities was investigated in detail. The photocatalytic active species for RhB degradation were revealed. Discussed the influence of different crystal plane exposure on photocatalytic activity.

## 2. Experimental section

### 2.1. Materials

The chemicals involved in this work are analytical reagents without further purification, including acetic acid ( $\text{CH}_3\text{COOH}$ ), sodium tungstate dihydrate ( $\text{Na}_2\text{WO}_4 \cdot 2\text{H}_2\text{O}$ ), RhB, of which  $\text{Na}_2\text{WO}_4 \cdot 2\text{H}_2\text{O}$  and  $\text{Bi}(\text{NO}_3)_3 \cdot 5\text{H}_2\text{O}$  can be obtained from Aladdin Reagent Co., Ltd., (China) and Sinopharm Chemical Reagent Co., Ltd., (China), respectively.

### 2.2. Preparation of catalysts

#### 2.2.1. Synthesis of $\text{Bi}_2\text{WO}_6$ with oxygen vacancies

To prepare  $\text{Bi}_2\text{WO}_6$ , 20 mL of a  $0.175 \text{ mol L}^{-1}$   $\text{Na}_2\text{WO}_4 \cdot 2\text{H}_2\text{O}$  (99.5%) aqueous solution was slowly poured into 40 mL of a  $0.175 \text{ mol L}^{-1}$   $\text{Bi}(\text{NO}_3)_3 \cdot 5\text{H}_2\text{O}$  (99%) acetic acid solution and stirred for 1 h to uniformly disperse it. Then, it was transferred to a polytetrafluoroethylene-lined autoclave (100 mL) and reacted at  $160^\circ\text{C}$  for 12 h. The cooled suspension was filtered and washed, and then dried to obtain  $\text{Bi}_2\text{WO}_6$  with oxygen vacancies.

#### 2.2.2. Regulating oxygen vacancy defects

Oxygen vacancy concentration was regulated of the as-synthesized  $\text{Bi}_2\text{WO}_6$  by calcining at  $265^\circ\text{C}$ ,  $315^\circ\text{C}$ ,  $365^\circ\text{C}$  and  $415^\circ\text{C}$  for 1 h with heating rate of  $10^\circ\text{C min}^{-1}$ , respectively.

### 2.3. Characterization

X-ray diffractometer (Rigaku D/Max-2500PC X, Japan) was used to characterize the crystal structure of samples (Cu target,  $\text{K}\alpha$  radiation source,  $\lambda = 0.15406 \text{ nm}$ , tube voltage 36 kV, tube current 30 mA, scan rate  $2^\circ/\text{min}$ ,  $10^\circ\sim 80^\circ$  scan). The Raman spectra of the samples were measured by HORIBA Jobin Yvon, France. The surface composition of samples was analyzed by X-ray photoelectron spectroscopy (Thermo ESCALAB 250Xi, USA). Using a field emission scanning electron microscopy (SEM, JSM-6360LA, Japan) to observe sample morphology, the working voltage was 5 kV, and the magnification was 15,000 times. A transmission electron microscopy (TEM, JEM-2100, Japan) was used to observe the exposed crystal plane of the samples. Japan Electronics (JEOL, Japan) JES FA200 was used to detect oxygen vacancies. The UV-vis DRS of the samples were obtained by Shimadzu UV-2550 spectrophotometer (Japan) with a spectral range of 200–700 nm. The photoelectric performance test of samples was conducted by an electrochemical workstation (CHI1-660D). Ag/AgCl electrodes and platinum electrodes were used as reference and counter electrodes. A FTO ( $1 \text{ cm} \times 2 \text{ cm}$ ) was inserted into a  $40 \text{ g L}^{-1}$  sample suspension of iodine and acetone solution at a voltage of 12 V for 3 min to obtain a working electrode ( $1 \text{ cm} \times 1 \text{ cm}$ ). The light source was a 300 W Xe lamp and the electrolyte solution was  $0.1 \text{ mol L}^{-1}$  of  $\text{Na}_2\text{SO}_4$ .

### 2.4. Evaluation of photocatalytic activity

Photocatalytic activity of  $\text{Bi}_2\text{WO}_6$  before and after calcination was determined by the degradation of RhB solution under a 300 W Xe lamp. 50 mg of the photocatalyst was evenly dispersed in 50 mL RhB aqueous solution ( $10 \text{ mg L}^{-1}$ ), and magnetically stirred for 1 h in the dark to reach the adsorption-desorption equilibrium. After the Xe lamp was turned on, the photocatalytic activity test was started. Taking 2 mL aliquots of the suspension at regular intervals, the solids were removed by high-speed centrifugation. The absorbance of the sample at 450 nm to 650 nm was measured by a UV-visible spectrophotometer to evaluate the catalytic activity of the sample (UV1800PC, Aucy, Shanghai).

The experimental conditions for free radical capture experiments and cycling experiments were based on photocatalytic degradation experiments, but the free radical capture experiment was to add different active radical capture agents to the photocatalytic reaction system. The samples used in the cycle experiments were obtained by centrifugation and drying.

## 3. Results and discussions

### 3.1. Structure and morphology analysis

It can be observed from Fig. 1 that the  $\text{Bi}_2\text{WO}_6$  sample synthesized by hydrothermal method had the Aurvillius

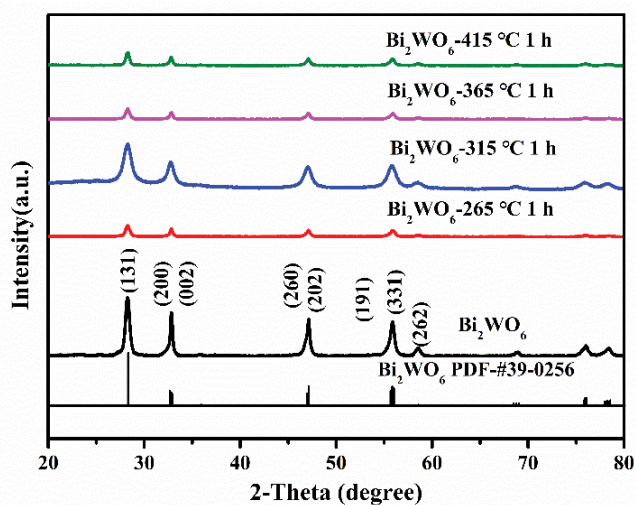


Fig. 1. X-ray diffraction patterns of  $\text{Bi}_2\text{WO}_6$  calcined at different temperatures.

crystal structure, and exhibited special anisotropic growth. Products calcined at different temperatures showed sharp distinctive diffraction peaks locating at  $2\theta = 28.30^\circ$ ,  $32.80^\circ$ ,  $47.14^\circ$ ,  $55.82^\circ$  and  $58.54^\circ$  [31,32], which are indexed to the (131), (200), (202), (331) and (262) crystal plane of orthorhombic  $\text{Bi}_2\text{WO}_6$  (JCPDS card No. 39-0256). In addition, after calcination, the half-width was significantly reduced, which indicates that calcination increases the grain size, suggesting that calcination may reduce the oxygen vacancy concentration. As can be seen from Figs. 2a and b, the size of  $\text{Bi}_2\text{WO}_6$  after calcination increased significantly, which is related to the thermodynamic mechanism of the material and may grow up during the annealing process. The particle size is usually inversely related to the defect concentration. This was consistent with the X-ray diffraction results [9]. After calcination, the particles of the sample become larger and the oxygen vacancy concentration decreases.

The morphologies and particle sizes of the prepared photocatalysts were characterized by SEM (Figs. 2a and b). It can be seen that the sample before calcination was a scattered block, with a small number of flakes wrapped by particles. After calcination, the sample was agglomerated into

large particles from nearly perpendicular nanoplates. As the annealing temperature increases, the particle size of  $\text{Bi}_2\text{WO}_6$  increases, which was consistent with the thermodynamic mechanism of the material. Although the sample was calcined and polymerized into large particles, the constituent parts have changed from the former block to the perpendicular flakes, which greatly increases its surface area.

EPR is one of the means to characterize oxygen vacancies. Unpaired electrons on the oxygen vacancies of the material will cause g to fluctuate at 2.001 [27,33]. The intensity of the EPR signal is related to the density of the oxygen vacancies [34]. As can be seen from Fig. 3a, the signal of  $\text{Bi}_2\text{WO}_6$  was strong, while the signal of  $\text{Bi}_2\text{WO}_6$ -315°C 1 h was weak. The  $\text{Bi}_2\text{WO}_6$  was prepared with acetic acid as the solvent was sealed during the preparation, and the oxygen concentration was low. Thus, the oxygen vacancy concentration was high. Due to calcination in an oxygen atmosphere, the oxygen vacancy concentration decreases after oxygen filling. Therefore, after the calcination of  $\text{Bi}_2\text{WO}_6$ , the EPR signal weakens. In order to identify the change in the number of oxygen vacancies during the calcination of  $\text{Bi}_2\text{WO}_6$ , Raman was used to characterizing all the prepared  $\text{Bi}_2\text{WO}_6$ . The Raman spectra of  $\text{Bi}_2\text{WO}_6$  before and after calcination are shown in Fig. 3b. It can be observed from Fig. 3b that  $\text{Bi}_2\text{WO}_6$  particles at 260, 290, 300, 418, 724, 798, 824  $\text{cm}^{-1}$  appeared vibrational bands. Among them, the peaks at 260, 290, 300  $\text{cm}^{-1}$ , the band at 418  $\text{cm}^{-1}$ , and the peaks at 798 and 824  $\text{cm}^{-1}$  corresponded to the apex and equatorial curvature of the O–W–O and the symmetrical and asymmetrical ends mode. The peak at 724  $\text{cm}^{-1}$  was related to the asymmetric bridging mode of the tungstate chain [17,35]. The half-width of  $\text{Bi}_2\text{WO}_6$  decreased with the increase of calcination temperature, which indicates that the number of oxygen vacancies on the surface of  $\text{Bi}_2\text{WO}_6$  decrease with calcination [18]. This was consistent with the EPR results. The local energy level formed by the oxygen vacancy defects at the bottom of the conduction band can significantly reduce the energy bandgap [17,36]. After calcination, because the number of oxygen vacancies decreased, the light absorption range decreased, the bandgap increased from 2.74 eV to 2.75 eV.

It is clearly seen from Fig. 4a that Bi, W and O were presented in  $\text{Bi}_2\text{WO}_6$ -315°C 1 h. In Figs. 4b–d, the X-ray photoelectron spectroscopy corresponded to the binding

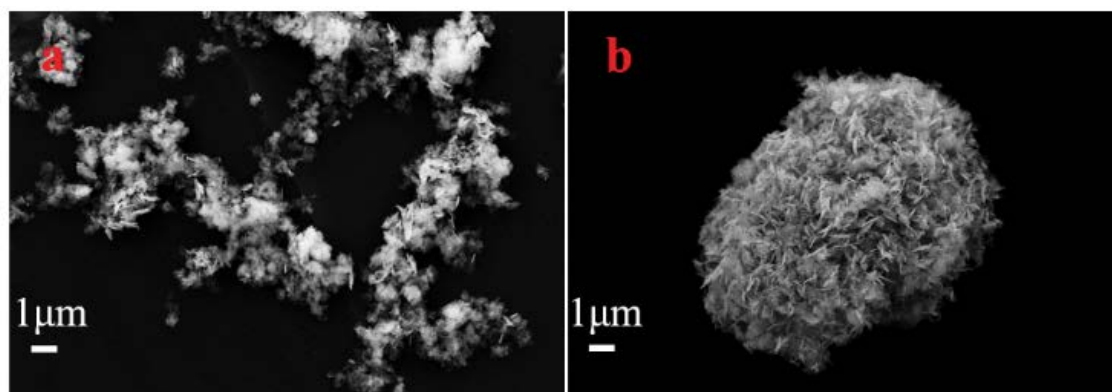


Fig. 2. Scanning electron microscopy images of (b)  $\text{Bi}_2\text{WO}_6$  and (c)  $\text{Bi}_2\text{WO}_6$ -315°C 1 h.

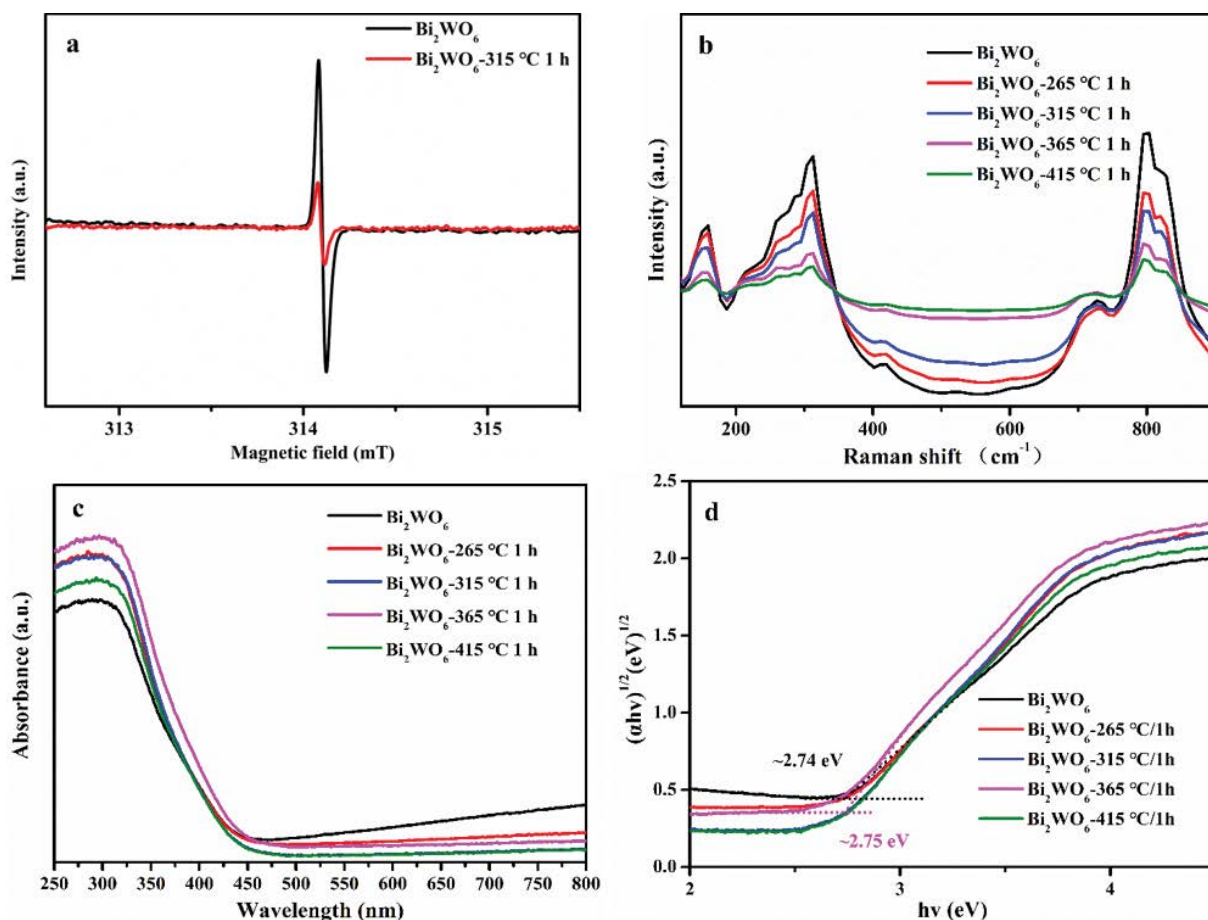


Fig. 3. (a) Electron paramagnetic resonance spectra of  $\text{Bi}_2\text{WO}_6$  before and after calcination, (b) Raman spectra of samples calcined at different temperatures, (c) UV-vis absorption spectra of  $\text{Bi}_2\text{WO}_6$  and  $\text{Bi}_2\text{WO}_6$  at different temperatures, and (d) bandgap energy.

energies of Bi 4f, W 4f and O 1s orbital in  $\text{Bi}_2\text{WO}_6$  before and after calcination, respectively. The binding energy of Bi 4f, W 4f and O 1s of the calcined  $\text{Bi}_2\text{WO}_6$  was transferred from 164.72 eV, 35.58 eV and 530.57 eV to lower binding energies, reaching 164.54 eV, 35.46 eV and 530.16 eV, which might be attributed to the weakening of the high electron effect of surface oxygen vacancies [36]. Table 1 shows the surface atomic ratios of Bi, W, and O in the  $\text{Bi}_2\text{WO}_6$  samples before and after calcination. It can be clearly observed that the O atomic ratio increased from 51.79% to 53.01% as the calcination temperature increased. Some oxygen vacancies may get O atoms during the calcination process. A proper amount of oxygen vacancies can help improve carrier separation efficiency.

It can be observed from Fig. 5 that the  $\text{Bi}_2\text{WO}_6$  before and after calcination were stacked via many nanosheets.  $\text{Bi}_2\text{WO}_6$ -315°C 1 h differed from  $\text{Bi}_2\text{WO}_6$  in some important ways. Obviously, the structure of  $\text{Bi}_2\text{WO}_6$ -315°C for 1 h is densely stacked with smaller layers, which is agreed well with the above SEM characterizations. The lattice fringes at inter-planar distance of 0.28 nm and 0.32 nm belong to the (200) and (131) crystal planes of  $\text{Bi}_2\text{WO}_6$ , respectively [16]. The high-resolution transmission electron microscopy images depicted that the exposure probability of the crystal plane (131) increased after

Table 1  
X-ray photoelectron spectroscopy analysis of surface components of  $\text{Bi}_2\text{WO}_6$  before and after calcination

Catalysts	Bi%	O%	W%	C%
$\text{Bi}_2\text{WO}_6$	20.32%	51.79%	10.34%	17.55%
$\text{Bi}_2\text{WO}_6$ -315°C 1 h	22.81%	53.01%	9.35%	14.84%

calcination. Thus, it is expected that the calcination is advantageous for the exposure of (131) facets.

### 3.2. Photocatalytic performance test

The activities of  $\text{Bi}_2\text{WO}_6$ ,  $\text{Bi}_2\text{WO}_6$ -265°C 1 h,  $\text{Bi}_2\text{WO}_6$ -315°C 1 h,  $\text{Bi}_2\text{WO}_6$ -365°C 1 h, and  $\text{Bi}_2\text{WO}_6$ -415°C 1 h were compared through photocatalytic degradation of RhB under light illumination. Firstly, magnetically stirred for 1 h in the dark to reach the adsorption-desorption equilibrium. After the dark reaction,  $\text{Bi}_2\text{WO}_6$ ,  $\text{Bi}_2\text{WO}_6$ -265°C 1 h,  $\text{Bi}_2\text{WO}_6$ -315°C 1 h,  $\text{Bi}_2\text{WO}_6$ -365°C 1 h and  $\text{Bi}_2\text{WO}_6$ -415°C 1 h adsorbed 11.3%, 19.4%, 21.7%, 15.6% and 16.3% of RhB, respectively, suggesting that calcination apparently improved the adsorption ability of  $\text{Bi}_2\text{WO}_6$  towards RhB. It was also confirmed in the subsequent  $\text{N}_2$  sorption isotherms.

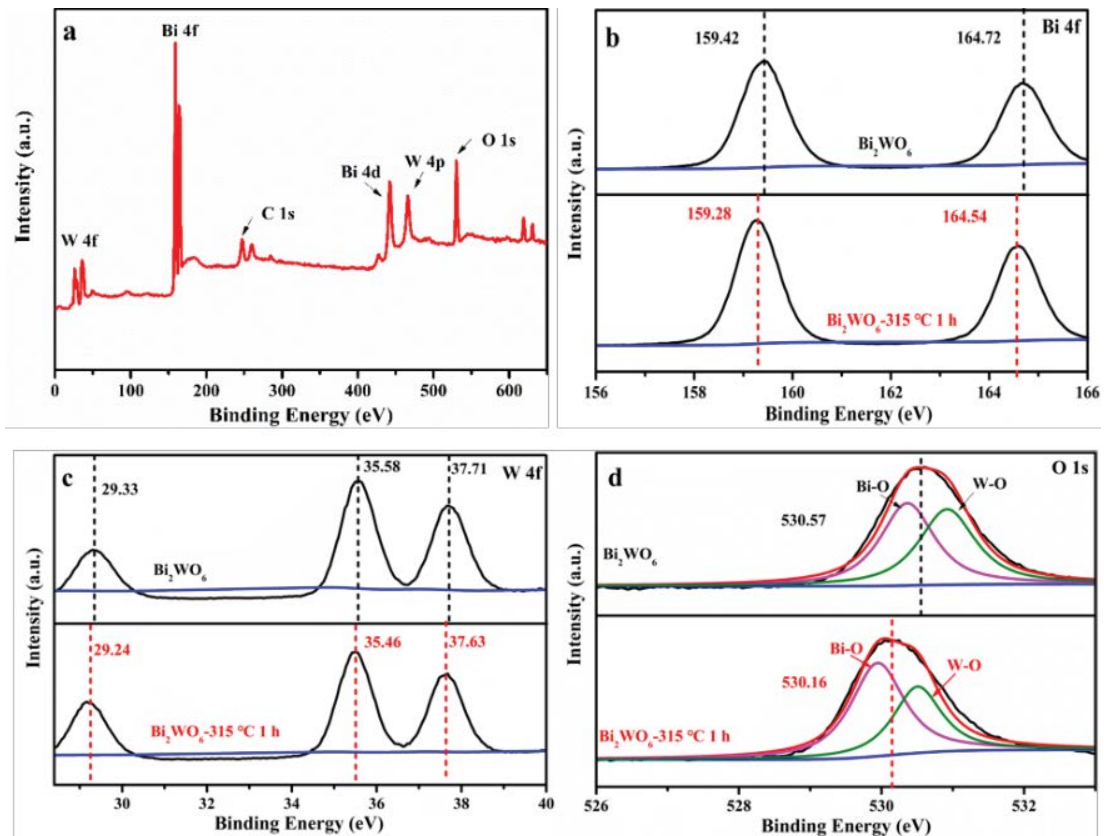


Fig. 4. (a) Full scan X-ray photoelectron spectroscopy of for  $\text{Bi}_2\text{WO}_6$ -315°C 1 h, (b) Bi 4f, (c) W 4f and (d) O 1s spectrum for  $\text{Bi}_2\text{WO}_6$  and  $\text{Bi}_2\text{WO}_6$ -315°C 1 h.

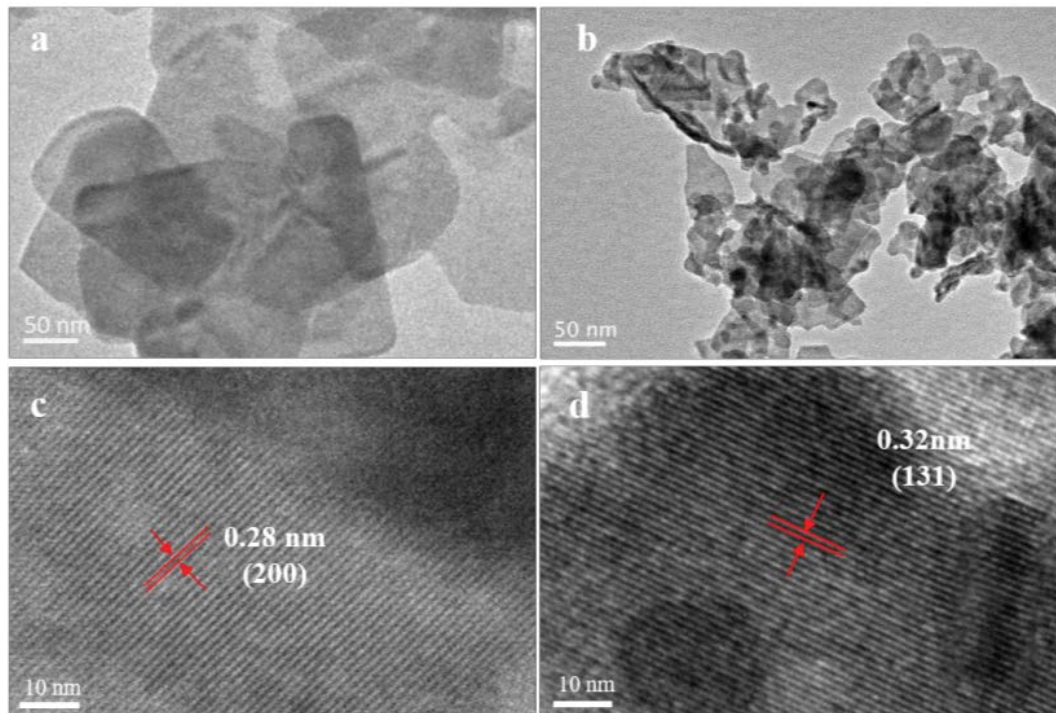


Fig. 5. Transmission electron microscopy and high-resolution transmission electron microscopy images of (a,c)  $\text{Bi}_2\text{WO}_6$  and (b,d)  $\text{Bi}_2\text{WO}_6$ -315°C 1 h.

It can be observed that the photocatalytic activity of the calcined sample was improved. After 3 h of irradiation, the photodegradation efficiency of RhB over  $\text{Bi}_2\text{WO}_6$  was 24%. When the calcination temperature increased from 265°C to 415°C, the degradation rates of RhB over  $\text{Bi}_2\text{WO}_6$ -265°C 1 h,  $\text{Bi}_2\text{WO}_6$ -315°C 1 h,  $\text{Bi}_2\text{WO}_6$ -365°C 1 h and  $\text{Bi}_2\text{WO}_6$ -415°C 1 h were 49%, 98%, 78% and 72%, respectively, indicating that the sample has the highest photocatalytic efficiency when the calcination temperature is 315°C. In more detail, the degradation velocity of the sample calcined at 315°C during the degradation of RhB was 21.4 times that of the pure sample. This is because calcination reduces the abundance of oxygen vacancies in  $\text{Bi}_2\text{WO}_6$ . Excess oxygen vacancies will become recombination of electrons and holes. Calcination adjusted the concentration of oxygen vacancies and improved photoelectric separation efficiency. The removal rates of total organic carbon and total oxidized nitrogen (TON) reached 46% and 65% over  $\text{Bi}_2\text{WO}_6$ -315°C 1 h, respectively (Fig. 6c). This showed that the sample has good mineralization and denitrification capabilities, and RhB has been effectively degraded. The stability test of the photocatalyst was carried out by recovering the photocatalyst after the reaction under the same experimental conditions (Fig. 6d). After five cycles, the photocatalytic activity of  $\text{Bi}_2\text{WO}_6$ -315°C 1 h slightly decreased, and the degradation rate of RhB was reduced from 98% to 64%.

After five cycles, the intensity of I(131)/I(200) decreased from 1.61 to 1.30 (Fig. 7a), and the probability of exposure of the (131) crystal face of the sample after the cycle decreased (Fig. 7b). It is proved from the side that the exposure of a crystal face (131) is beneficial to the improvement of photocatalytic efficiency.

### 3.3. Mechanisms of enhanced photocatalytic activity

It can be seen from the adsorption-desorption curve that  $\text{Bi}_2\text{WO}_6$  and  $\text{Bi}_2\text{WO}_6$ -315°C 1 h are typical type IV isotherms, their hysteresis loops are between 0.7–1.0 ( $H_3$ ) and their specific surface areas were respectively 17.00 and 18.83  $\text{m}^2 \text{g}^{-1}$ . The specific surface area of  $\text{Bi}_2\text{WO}_6$ -315°C for 1 h is about 1.11 times that of  $\text{Bi}_2\text{WO}_6$ . The relationship between the relative pressure of nitrogen and its condensed curvature in the pore can be expressed by Kelvin's equation, as shown in Eq. (1).

$$r_k = -\frac{2\sigma_1 V_{m1}}{RT_b \ln \frac{P}{P_0}} \quad (1)$$

In Eq. (1):  $r_k$  is the radius of curvature of the adsorbed gas condensed in the pores;  $\sigma_1$  is the surface tension of liquid nitrogen (0.0088760  $\text{N m}^{-1}$ );  $V_{m1}$  is the molar volume of

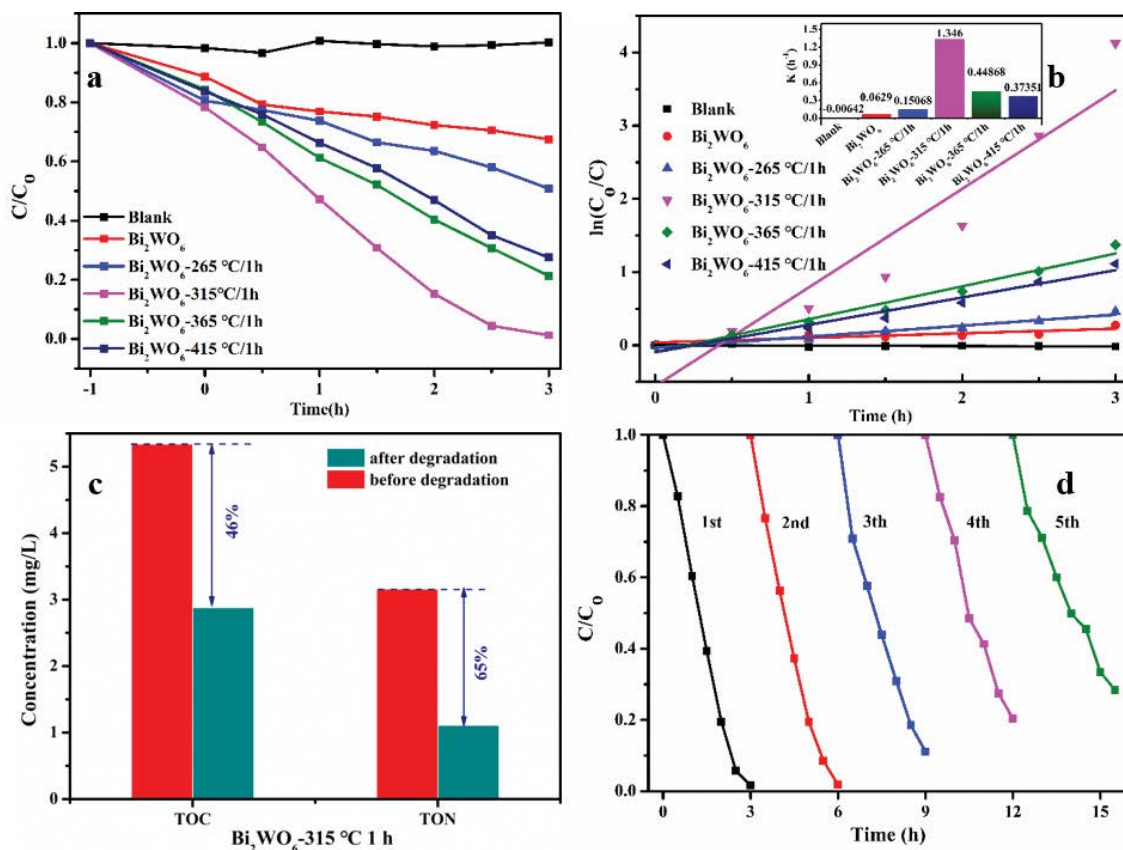


Fig. 6. (a) Photocatalytic degradation of RhB over different samples under light irradiation, (b) kinetic curves of photocatalytic processes of different materials, (c) total organic carbon and TON removal efficiency of RhB over  $\text{Bi}_2\text{WO}_6$ -315°C 1 h, and (d) dynamic curve of RhB cycling test of  $\text{Bi}_2\text{WO}_6$ -315°C 1 h.

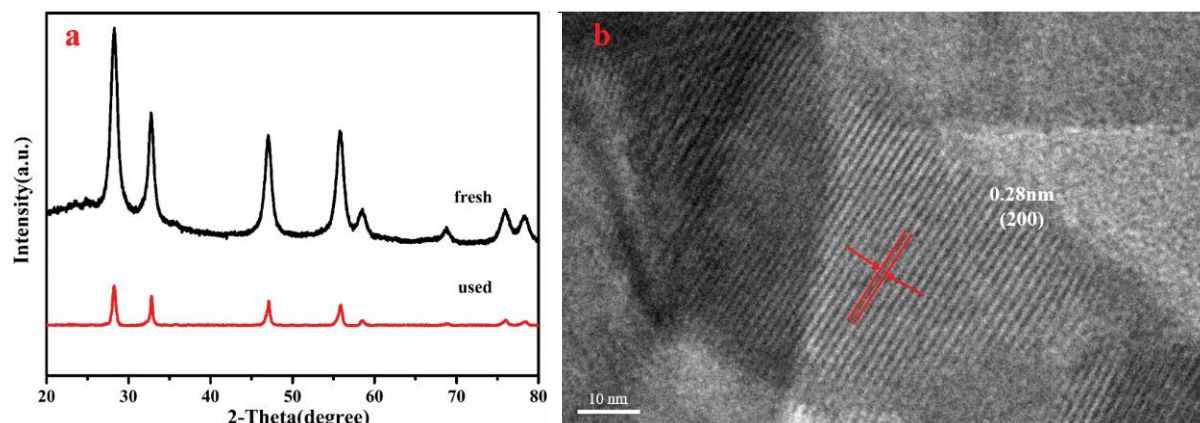


Fig. 7. (a) X-ray diffraction patterns and (b) transmission electron microscopy images of Bi<sub>2</sub>WO<sub>6</sub>-315°C 1 h used before and after.

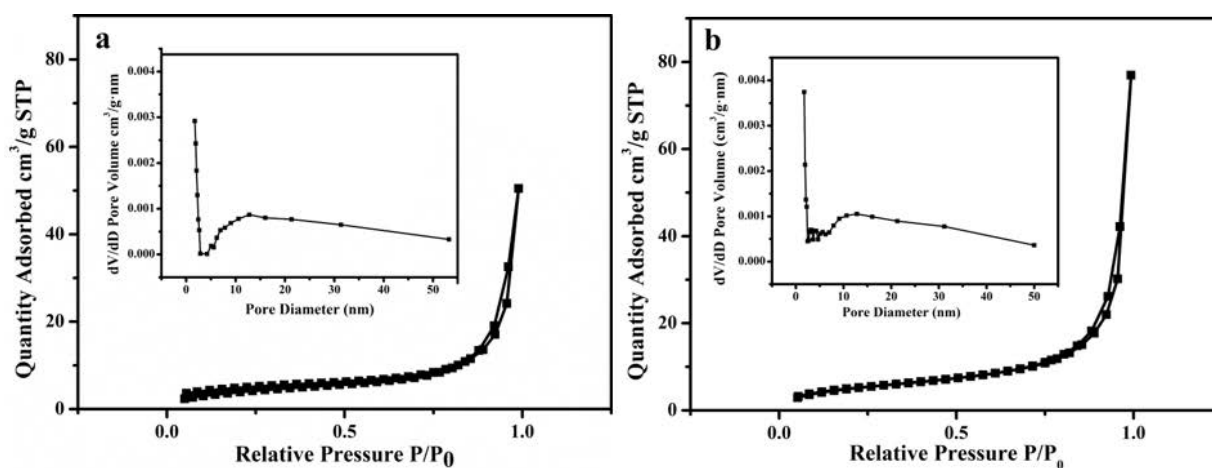


Fig. 8. Nitrogen adsorption–desorption isotherms and pore size distribution curves for (a) Bi<sub>2</sub>WO<sub>6</sub> and (b) Bi<sub>2</sub>WO<sub>6</sub>-315°C 1 h. Insets: the corresponding pore size distributions.

liquid nitrogen of the liquid condensate ( $0.034752 \text{ L mol}^{-1}$ );  $R$  is the gas constant ( $8.314 \text{ J mol}^{-1} \text{ K}^{-1}$ );  $T_b$  is the temperature of the cold bath ( $77.35 \text{ K}$ ) during analysis and testing.

SEM showed that after calcination, the flakes in the sample increased significantly, which may be the reason for the increase in surface area and decrease in pore size. The larger specific surface increases its chance of contact with pollutants, and the pore structure is conducive to the diffusion and circulation of pollutant molecules inside them [37]. Thus, photocatalytic performance of Bi<sub>2</sub>WO<sub>6</sub>-315°C 1 h is better.

Fig. 9a illustrates light photocurrent Bi<sub>2</sub>WO<sub>6</sub> and Bi<sub>2</sub>WO<sub>6</sub>-315°C 1 h. Both Bi<sub>2</sub>WO<sub>6</sub> and Bi<sub>2</sub>WO<sub>6</sub>-315°C 1 h exhibited rapid light response photocurrent. The photocurrent intensity of Bi<sub>2</sub>WO<sub>6</sub>-315°C 1 h is significantly higher than that of Bi<sub>2</sub>WO<sub>6</sub>, which proves that excessive oxygen vacancies may become the recombination center of electrons and holes, and an appropriate amount of oxygen vacancies become the recombination centers of electrons and holes can act as photo-induced charge traps and inhibit electron-hole recombination and accelerate transportation [38,39]. The electrochemical impedance spectroscopy (EIS) results (Fig. 9b) were consistent with the photocurrent results. The calcined sample had

a smaller impedance radius, indicating a higher charge separation capability [40–44]. Table 2 summarizes the charge transfer resistance ( $R_{ct}$ ) simulation results of Bi<sub>2</sub>WO<sub>6</sub> calcined at different temperatures based on EIS data. It can be observed that Bi<sub>2</sub>WO<sub>6</sub>-315°C 1 h has the lowest charge transfer resistance and the highest charge transfer efficiency. The photoluminescence (PL) spectrum showed that the calcined sample exhibits a reduced PL signal, which further proved that the calcining can improve the separation efficiency of electrons and holes (Fig. S2). This is because calcination increases the specific surface area of Bi<sub>2</sub>WO<sub>6</sub>, making it have a smaller charge transport resistance and higher photoelectric conversion efficiency. Although the light absorption range of the sample was slightly reduced after calcination, the photocatalytic activity of the sample was still significantly enhanced due to the greatly improved photoelectric separation efficiency.

#### 3.4. Active species for photocatalytic degradation of RhB

In order to further discuss the effects of active species, we added different types of sacrificial agents to the catalytic system. Isopropyl alcohol (IPA) is a capture agent of

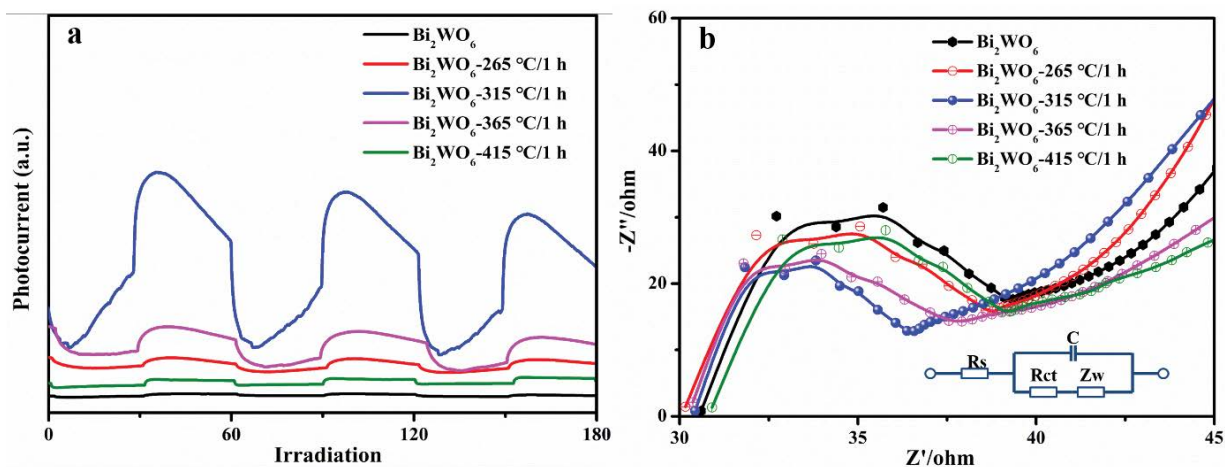


Fig. 9. (a) Photocurrent response and (b) EIS spectra of  $\text{Bi}_2\text{WO}_6$  calcined at different temperatures.

Table 2  
 $R_{ct}$  parameters of calcined samples at different temperatures

Samples	$R_{ct}$ ( $\Omega$ )
$\text{Bi}_2\text{WO}_6$	36.39
$\text{Bi}_2\text{WO}_6$ -265°C 1 h	9.04
$\text{Bi}_2\text{WO}_6$ -315°C 1 h	0.25
$\text{Bi}_2\text{WO}_6$ -365°C 1 h	7.25
$\text{Bi}_2\text{WO}_6$ -415°C 1 h	8.94

$\cdot\text{OH}$ . Ethylenediaminetetraacetic acid disodium (EDTA-2Na) is a sacrificial agent of  $\text{h}^+$  and the benzoquinone (BQ) is a capture agent of  $\cdot\text{O}_2^-$ . The amount of capture agent was  $0.1 \text{ mmol L}^{-1}$ . After adding different capture agents, the degradation rate of RhB is shown in Fig. 10. The IPA did not change the degradation rate of RhB. The BQ and EDTA significantly reduced the activity of the catalyst. The results indicated that  $\cdot\text{O}_2^-$  and  $\text{h}^+$  played an important role in the photocatalytic degradation of RhB. Electron spin

resonance (ESR) spectroscopy with 2,2-dimethyl-3,4-dihydro-2H-pyrrole-1-oxide (DMPO) spin-trapping adducts was adopted to further confirm the role of certain active species in the reaction system. As shown in Fig. 10b, a typical six-peak signal was detected under visible light which can be assigned to the characteristic signals of DMPO- $\cdot\text{O}_2^-$  adduct, whereas no signal was found in dark condition, which confirmed that  $\cdot\text{O}_2^-$  could be generated in the photocatalytic degradation process over  $\text{Bi}_2\text{WO}_6$ -315°C 1 h.

Too much oxygen vacancies will become the center of electron and hole recombination. After the oxygen vacancies were reduced by calcination, the oxygen vacancies will capture a part of electrons to promote the separation of electrons and holes. Among them, electrons and oxygen adsorbed on the catalyst surface were generated  $\cdot\text{O}_2^-$  and separated  $\text{h}^+$  become the main active species for degradation of RhB.

#### 4. Conclusions

In short,  $\text{Bi}_2\text{WO}_6$  nanosheets with oxygen vacancies were successfully prepared, and the number of oxygen vacancies

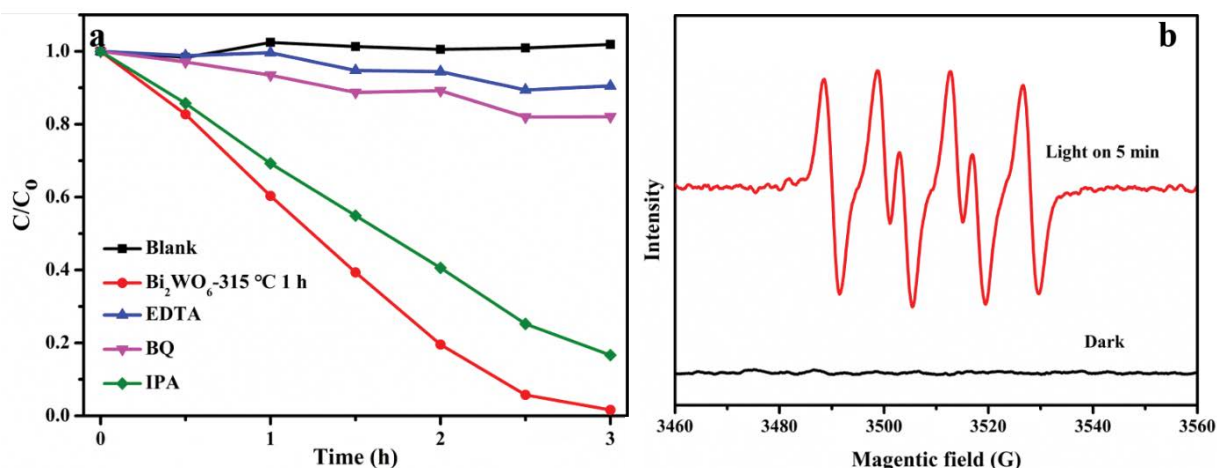


Fig. 10. (a) Effect of capture agents on the catalytic activity and DMPO spin-trapping ESR spectra for DMPO- $\cdot\text{O}_2^-$  of  $\text{Bi}_2\text{WO}_6$ -315°C 1 h.

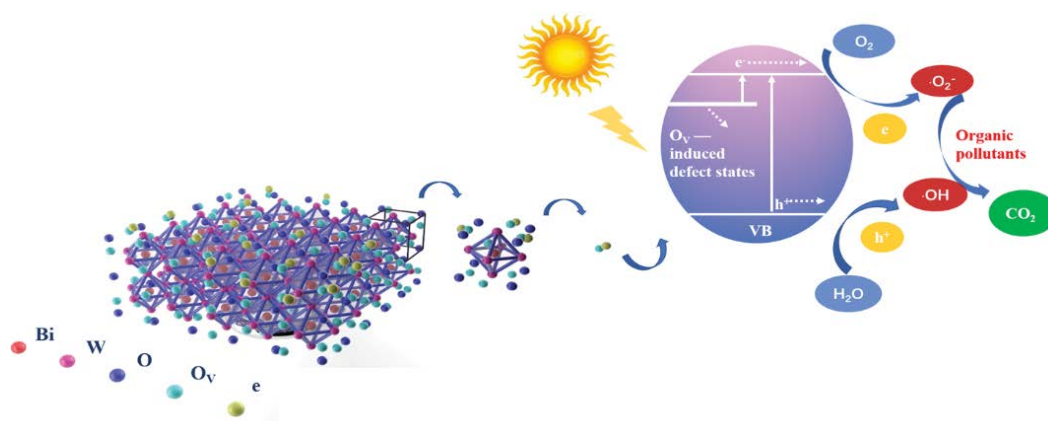


Fig. 11. Construction of oxygen vacancy  $\text{Bi}_2\text{WO}_6$  and the mechanism diagram of enhanced photocatalytic activity.

was reduced by calcination to obtain the optimal concentration of oxygen vacancies while increasing the specific surface area. This suppresses the  $\text{Bi}_2\text{WO}_6$  electron-hole recombination, extends the carrier lifetime, reduces the charge transport resistance, and improves the photoelectric conversion efficiency. Thus, the photocatalytic activity of  $\text{Bi}_2\text{WO}_6$  was greatly improved.

#### Acknowledgments

This work was supported by the National Natural Science Foundation of China [21876015]; the Natural Science Foundation of Jiangsu Province [BK20161277] and [BK20190934]; the Natural Science Foundation of Jiangsu Education Department [16KJB610002]; the Postdoctoral Science Foundation of China [2017M611784]; and the Natural Science Foundation of Jiangsu Higher Education Institutions [20KJA50007].

#### References

- [1] G.M. Neelgund, V.N. Bliznyuk, A. Oki, Photocatalytic activity and NIR laser response of polyaniline conjugated graphene nanocomposite prepared by a novel acid-less method, *Appl. Catal., B*, 187 (2016) 357–366.
- [2] M. Shaban, M.R. Abukhadra, S.S. Ibrahim, M.G. Shahien, Photocatalytic degradation and photo-Fenton oxidation of Congo red dye pollutants in water using natural chromite—response surface optimization, *Appl. Water Sci.*, 7 (2017) 4743–4756.
- [3] M. Shaban, M.R. Abukhadra, A. Hamd, R.R. Amin, A. Abdel Khalek, Photocatalytic removal of Congo red dye using MCM-48/ $\text{Ni}_2\text{O}_3$  composite synthesized based on silica gel extracted from rice husk ash; fabrication and application, *J. Environ. Manage.*, 204 (2017) 189–199.
- [4] S. Tamilselvi, M. Asaithambi, P. Sivakumar, Nano- $\text{TiO}_2$ -loaded activated carbon fiber composite for photodegradation of a textile dye, *Desal. Water Treat.*, 57 (2015) 15495–15502.
- [5] Y.X. Yan, H. Yang, Z. Yi, T. Xian, R.S. Li, X.X. Wang, Construction of  $\text{Ag}_2\text{S}@/\text{CaTiO}_3$  heterostructure photocatalysts for enhanced photocatalytic degradation of dyes, *Desal. Water Treat.*, 170 (2019) 349–360.
- [6] S. Rajendran, M.M. Khan, F. Gracia, J.Q. Qin, V.K. Gupta, S. Arumainathan,  $\text{Ce}^{3+}$ -ion-induced visible-light photocatalytic degradation and electrochemical activity of  $\text{ZnO}/\text{CeO}_2$  nanocomposite, *Sci. Rep.-UK*, 6 (2016) 31641.
- [7] X.L. Wu, M. Fu, P. Lu, Q.Y. Ren, C. Wang, Unique electronic structure of Mg/O co-decorated amorphous carbon nitride enhances the photocatalytic tetracycline hydrochloride degradation, *Chin. J. Catal.*, 40 (2019) 776–785.
- [8] N. Chaibakhsh, N. Ahmadi, M.A. Zanjanchi, Optimization of photocatalytic degradation of neutral red dye using  $\text{TiO}_2$  nanocatalyst via Box–Behnken design, *Desal. Water Treat.*, 57 (2016) 9296–9306.
- [9] W.C. Huo, X. Dong, J.Y. Li, M. Liu, X.Y. Liu, Y.X. Zhang, F. Dong, Synthesis of  $\text{Bi}_2\text{WO}_6$  with gradient oxygen vacancies for highly photocatalytic NO oxidation and mechanism study, *Chem. Eng. J.*, 361 (2019) 129–138.
- [10] W.N. Xu, C.H. Zheng, H. Hua, Q. Yang, L. Chen, Y. Xi, C.G. Hu, Synthesis and photoelectrochemical properties of  $\text{CdWO}_4$  and  $\text{CdS}/\text{CdWO}_4$  nanostructures, *Appl. Surf. Sci.*, 327 (2015) 140–148.
- [11] Y.-C. Zhang, Z. Li, L. Zhang, L. Pan, X.W. Zhang, L. Wang, Fazal-e-Aleem, J.-J. Zou, Role of oxygen vacancies in photocatalytic water oxidation on ceria oxide: experiment and DFT studies, *Appl. Catal., B*, 224 (2018) 101–108.
- [12] Y. Zhang, W.Q. Cui, W.J. An, L. Liu, Y.H. Liang, Y.F. Zhu, Combination of photoelectrocatalysis and adsorption for removal of bisphenol A over  $\text{TiO}_2$ -graphene hydrogel with 3D network structure, *Appl. Catal., B*, 221 (2018) 36–46.
- [13] R. Saravanan, M. Mansoob Khan, V.K. Gupta, E. Mosquera, F. Gracia, V. Narayanan, A. Stephen,  $\text{ZnO}/\text{Ag}/\text{CdO}$  nanocomposite for visible light-induced photocatalytic degradation of industrial textile effluents, *J. Colloid Interface Sci.*, 452 (2015) 126–133.
- [14] Z. Liu, X.Q. Liu, C.L. Yu, L.F. Wei, H.B. Ji, Fabrication and characterization of I doped  $\text{Bi}_2\text{MoO}_6$  microspheres with distinct performance for removing antibiotics and Cr(VI) under visible light illumination, *Sep. Purif. Technol.*, 247 (2020) 116951.
- [15] C.L. Yu, Z. Wu, R.Y. Liu, D.D. Dionysiou, K. Yang, C.Y. Wang, H. Liu, Novel fluorinated  $\text{Bi}_2\text{MoO}_6$  nanocrystals for efficient photocatalytic removal of water organic pollutants under different light source illumination, *Appl. Catal., B*, 209 (2017) 1–11.
- [16] Y.E. Kitaev, M.I. Aroyo, J.M. Perez-Mato, Site symmetry approach to phase transitions in perovskite-related ferroelectric compounds, *Phys. Rev.*, 75 (2007) 064110.
- [17] J.G. Hou, S.Y. Cao, Y.Z. Wu, F. Liang, Y.F. Sun, Z.S. Lin, L.C. Sun, Simultaneously efficient light absorption and charge transport of phosphate and oxygen-vacancy confined in bismuth tungstate atomic layers triggering robust solar  $\text{CO}_2$  reduction, *Nano Energy*, 32 (2017) 359–366.
- [18] N. Zhang, R. Ciriminna, M. Pagliaro, Y.-J. Xu, Nanochemistry-derived  $\text{Bi}_2\text{WO}_6$  nanostructures: towards production of sustainable chemicals and fuels induced by visible light, *Chem. Soc. Rev.*, 43 (2014) 5276–5287.
- [19] C.L. Yu, H.B. He, Q.Z. Fan, W.Y. Xie, Z. Liu, H.B. Ji, Novel B-doped  $\text{BiOCl}$  nanosheets with exposed (001) facets and photocatalytic mechanism of enhanced degradation efficiency for organic pollutants, *Sci. Total Environ.*, 694 (2019) 133727, <https://doi.org/10.1016/j.scitotenv.2019.133727>.

- [20] D.B. Zeng, C.L. Yu, Q.Z. Fan, J.L. Zeng, L.F. Wei, Z.S. Li, K. Yang, H.B. Ji, Theoretical and experimental research of novel fluorine doped hierarchical  $\text{Sn}_3\text{O}_4$  microspheres with excellent photocatalytic performance for removal of Cr(VI) and organic pollutants, *Chem. Eng. J.*, 391 (2020) 123607, <https://doi.org/10.1016/j.cej.2019.123607>.
- [21] C.L. Yu, H.B. He, X.Q. Liu, J.L. Zeng, Z. Liu, Novel  $\text{SiO}_2$  nanoparticle-decorated  $\text{BiOCl}$  nanosheets exhibiting high photocatalytic performances for the removal of organic pollutants, *Chin. J. Catal.*, 40 (2019) 1212–1221.
- [22] C.L. Yu, F.Y. Chen, D.B. Zeng, Y. Xie, W.Q. Zhou, Z. Liu, L.F. Wei, K. Yang, D.H. Li, A facile phase transformation strategy for fabrication of novel Z-scheme ternary heterojunctions with efficient photocatalytic properties, *Nanoscale*, 11 (2019) 7720–7733.
- [23] Y.Y. Zhang, L.L. Wang, X.Y. Kong, H.Y. Jiang, F. Zhang, J.S. Shi, Novel Ag-Cu bimetallic alloy decorated near-infrared responsive three-dimensional rod-like architectures for efficient photocatalytic water purification, *J. Colloid Interface Sci.*, 522 (2018) 29–39.
- [24] Y. Li, X.Y. Wu, J. Li, K. Wang, G.K. Zhang, Z-scheme  $\text{g-C}_3\text{N}_4/\text{Cs}_2\text{WO}_3$  heterostructure as smart window coating for UV isolating, Vis penetrating, NIR shielding and full spectrum photocatalytic decomposing VOCs, *Appl. Catal., B*, 229 (2018) 218–226.
- [25] J.G. Wang, H. Liang, C. Zhang, B. Jin, Y. Men,  $\text{Bi}_2\text{WO}_6$ -nanosheets with tunable Bi quantum dots and oxygen vacancies for photocatalytic selective oxidation of alcohols, *Appl. Catal., B*, 256 (2019) 117874, <https://doi.org/10.1016/j.apcatb.2019.117874>.
- [26] M.L. Sun, X. Dong, B. Lei, J.Y. Li, P. Chen, Y.X. Zhang, F. Dong, Graphene oxide mediated co-generation of C-doping and oxygen defects in  $\text{Bi}_2\text{WO}_6$  nanosheets: a combined DRIFTS and DFT investigation, *Nanoscale*, 11 (2019) 20562–20570.
- [27] H. Chen, C.T. Zhang, Y. Pang, Q.H. Shen, Y. Yu, Y.X. Su, J.B. Wang, F. Zhang, H. Yang, Oxygen vacancy regulation in Nb-doped  $\text{Bi}_2\text{WO}_6$  for enhanced visible light photocatalytic activity, *RSC Adv.*, 9 (2019) 22559–22566.
- [28] Y. Liu, B. Wei, L.L. Xu, H. Gao, M.Y. Zhang, Generation of oxygen vacancy and OH radicals: a comparative study of  $\text{Bi}_2\text{WO}_6$  and  $\text{Bi}_2\text{WO}_6$ -nanoplates, *ChemCatChem*, 7 (2015) 4076–4084.
- [29] J.Q. Li, Z. Liang, Y. Qin, L. Guo, N. Lei, Q.Q. Song, Defective  $\text{Bi}_2\text{WO}_6$ -supported Cu nanoparticles as efficient and stable photoelectrocatalytic for water splitting in near-neutral media, *Energy Technol.*, 6 (2018) 2247–2255.
- [30] Y.X. Yan, H. Yang, Z. Yi, X.X. Wang, R.S. Li, T. Xian, Evolution of Bi nanowires from  $\text{BiOBr}$  nanoplates through a  $\text{NaBH}_4$  reduction method with enhanced photodegradation performance, *Environ. Eng. Sci.*, 37 (2019) 64–77.
- [31] D. Sun, Y. Le, C.J. Jiang, B. Cheng, Ultrathin  $\text{Bi}_2\text{WO}_6$  nanosheet decorated with Pt nanoparticles for efficient formaldehyde removal at room temperature, *Appl. Surf. Sci.*, 441 (2018) 429–437.
- [32] Q.-S. Wu, Y. Cui, L.-M. Yang, G.-Y. Zhang, D.-Z. Gao, Facile *in-situ* photocatalysis of  $\text{Ag}/\text{Bi}_2\text{WO}_6$  heterostructure with obviously enhanced performance, *Sep. Purif. Technol.*, 142 (2015) 168–175.
- [33] N. Zhang, X.Y. Li, H.C. Ye, S.M. Chen, H.X. Ju, D.B. Liu, Y. Lin, W. Ye, C.M. Wang, Q. Xu, J.F. Zhu, L. Song, J. Jiang, Y.J. Xiong, Oxide defect engineering enables to couple solar energy into oxygen activation, *J. Am. Chem. Soc.*, 138 (2016) 8928–8935.
- [34] H. Li, J.G. Shi, K. Zhao, L.Z. Zhang, Sustainable molecular oxygen activation with oxygen vacancies on the {001} facets of  $\text{BiOCl}$  nanosheets under solar light, *Nanoscale*, 6 (2014) 14168–14173.
- [35] S.S. Zhang, W.H. Pu, H. Du, Y.Y. Wang, C.Z. Yang, J.Y. Gong, Facile synthesis of Pt assisted  $\text{Bi-Bi}_2\text{WO}_6$  with oxygen vacancies for the improved photocatalytic activity under visible light, *Appl. Surf. Sci.*, 459 (2018) 363–375.
- [36] X.Y. Kong, Y.Y. Choo, S.-P. Chai, A.K. Soh, A.R. Mohamed, Oxygen vacancy induced  $\text{Bi}_2\text{WO}_6$  for the realization of photocatalytic  $\text{CO}_2$  reduction over the full solar spectrum: from the UV to the NIR region, *Chem. Commun.*, 52 (2016) 14242–14245.
- [37] N. Huang, Z.P. Qu, C. Dong, Y. Qin, X.X. Duan, Superior performance of  $\alpha/\beta\text{-MnO}_2$  for the toluene oxidation: active interface and oxygen vacancy, *Appl. Catal., A*, 560 (2018) 195–205.
- [38] Z.M. Chen, J.G. Wang, G.J. Zhai, W. An, Y. Men, Hierarchical yolk-shell  $\text{WO}_3$  microspheres with highly enhanced photoactivity for selective alcohol oxidations, *Appl. Catal., B*, 218 (2017) 825–832.
- [39] J.G. Wang, Z.M. Chen, G.J. Zhai, Y. Men, Boosting photocatalytic activity of  $\text{WO}_3$  nanorods with tailored surface oxygen vacancies for selective alcohol oxidations, *Appl. Surf. Sci.*, 462 (2018) 760–771.
- [40] C.L. Yu, D.B. Zeng, Q.Z. Fan, K. Yang, J. Zeng, L.F. Wei, J.H. Yi, H.B. Ji, The distinct role of boron doping in  $\text{Sn}_3\text{O}_4$  microspheres for synergistic removal of phenols and Cr(VI) in simulated wastewater, *Environ. Sci.: Nano*, 7 (2020) 286–303.
- [41] Q. Quan, S.J. Xie, B. Weng, Y. Wang, Y.-J. Xu, Revealing the double-edged sword role of graphene on boosted charge transfer versus active site control in  $\text{TiO}_2$  nanotube arrays@ $\text{RGO}/\text{MoS}_2$  heterostructure, *Small*, 14 (2018) 1704531, <https://doi.org/10.1002/smll.201704531>.
- [42] L.M. Sun, L. Xiang, X. Zhao, C.-J. Jia, J. Yang, Z. Jin, X.F. Cheng, W.L. Fan, Enhanced visible-light photocatalytic activity of  $\text{BiOI}/\text{BiOCl}$  heterojunctions: key role of crystal facet combination, *ACS Catal.*, 5 (2015) 3540–3551.
- [43] J.L. Xu, C.F. Sun, Z.Y. Wang, Y.D. Hou, Z.X. Ding, S.B. Wang, Perovskite oxide  $\text{LaNiO}_3$  nanoparticles for boosting  $\text{H}_2$  evolution over commercial  $\text{CdS}$  with visible light, *Renewable Energy*, 24 (2018) 18512–18517.
- [44] M. Zhou, S.B. Wang, P.J. Yang, C.J. Huang, X.C. Wang, Boron carbon nitride semiconductors decorated with  $\text{CdS}$  nanoparticles for photocatalytic reduction of  $\text{CO}_2$ , *ACS Catal.*, 8 (2018) 4928–4936.

## Supplementary information

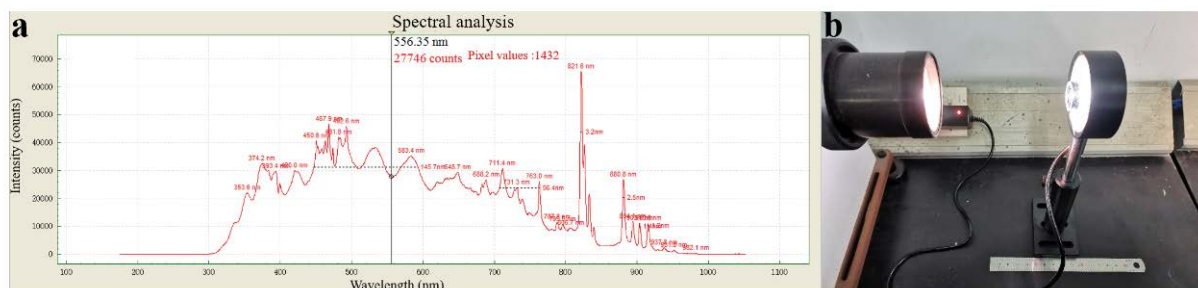
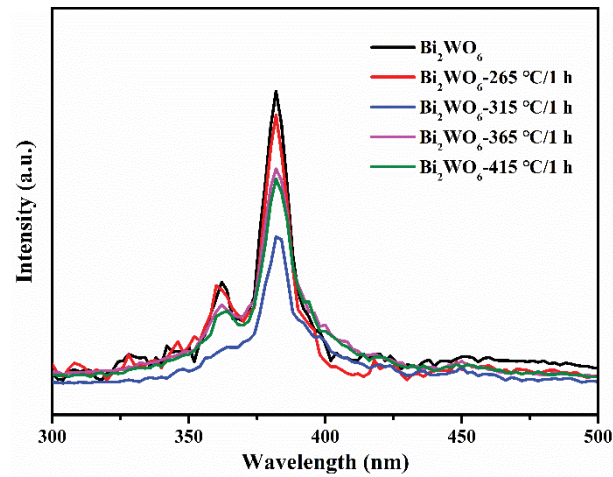


Fig. S1. (a) Sunlight spectrum and (b) light intensity test picture.

Table S1

Calculation experiment report of energy conversion efficiency and quantum yield of solar photocatalytic system

Beijing Zhongjiao Jinyuan Technology Co., Ltd., (Beijing, China) (GB/T26915-2011)	
Calculation experiment report of energy conversion efficiency and quantum yield of solar photocatalytic system	
Report time: 2020-09-20	
Experimental conditions and parameters	
Laboratory equipment	CEL-NP2000
Spot type	Round
Filter type	sunshine
Spot radius	2.5000 cm
Experimental results	
Average irradiance	2.0858E+004 W m <sup>-2</sup>
Reactor light area	1.9635E-003 m <sup>2</sup>
Average radiant flux of incident light (optical power)	4.0955E+001 W
Number of incident photons (photons incident within 1 h)	2.2267E+023

Fig. S2. PL spectra of Bi<sub>2</sub>WO<sub>6</sub> calcined at different temperatures.